Appl. Phys. B 90, 629–639 (2008)
DOI: 10.1007/s00340-007-2877-2

**Applied Physics B**
**Lasers and Optics**

M. HOFMANN[1]
B.F. KOCK[1]
T. DREIER[1,✉]
H. JANDER[2]
C. SCHULZ[1,3]

# Laser-induced incandescence for soot-particle sizing at elevated pressure

[1] IVG, Universität Duisburg–Essen, Lotharstraße 1, 47057 Duisburg, Germany
[2] IPC, Universität Göttingen, Göttingen, Germany
[3] CeNIDE, Center for Nanointegration Duisburg–Essen, Duisburg, Germany

**Received: 11 July 2007/Revised version: 22 October 2007**
**Published online: 13 December 2007 •** 

**ABSTRACT** This paper describes the applicability of laser-induced incandescence (LII) as a measurement technique for primary soot particle sizes at elevated pressure. A high-pressure burner was constructed that provides stable, laminar, sooting, premixed ethylene/air flames at 1–10 bar. An LII model was set up that includes different heat-conduction sub-models and used an accommodation coefficient of 0.25 for all pressures studied. Based on this model experimental time-resolved LII signals recorded at different positions in the flame were evaluated with respect to the mean particle diameter of a log-normal particle-size distribution. The resulting primary particle sizes were compared to results from TEM images of soot samples that were collected thermophoretically from the high-pressure flame. The LII results are in good agreement with the mean primary particle sizes of a log-normal particle-size distribution obtained from the TEM-data for all pressures, if the LII signals are evaluated with the heat-conduction model of Fuchs combined with an aggregate sub-model that describes the reduced heat conduction of aggregated primary soot particles. The model, called LIISim, is available online via a web interface.

**PACS** 65.80.+n; 78.20.Nv; 42.62.-b; 47.70.Pq

## 1 Introduction

Soot formation has been a major issue in combustion research over the last few decades as soot is emitted by many practical combustion processes, e.g. power plants and internal combustion engines. Soot is known to be a major pollutant and particle size is important in assessing health risks. Small particles are considered to be more dangerous than large particles because they can penetrate deeply into the lungs and are assumed to cause cancer, asthma, fibrosis, and allergies. Suitable diagnostics techniques for the in-situ measurement of particle sizes and volume fraction are required in order to understand and reduce the particle emission from combustion devices.

Laser-induced incandescence (LII) has proven to be a powerful tool for soot diagnostics. The LII signal is due to thermal radiation from particles that are heated by an intense laser pulse. Subsequent cooling occurs through several heat-loss channels until, typically after a few hundreds of nanoseconds, the particle temperature reaches ambient gas temperature again. LII is basically used for two applications: The determination of the volume fraction of gas-borne soot and in-situ particle sizing of primary soot particles. LII has been used successfully in a variety of systems for measuring volume fractions of soot in laminar diffusion flames [1–3], laminar premixed flames [4–7], and turbulent flames [1, 8–10]. Particle sizes have been deduced from the temporal behavior of the LII signal taking the ratio of the LII signal at two different delay times after the signal peak [11, 12] as well as using the entire decay curve in point measurements [6, 13–16]. Particle sizes were obtained assuming monodisperse particles [6, 14, 15] as well as considering a polydisperse log-normal particle-size distribution [13, 16]. A new workshop series on LII [17] started in 2005, and resulted in an overview of current state-of-the-art LII research [18].

Although many LII applications were performed under atmospheric pressure conditions, e.g. in laboratory flames, only limited investigations have been performed on LII at elevated pressures. In many practical combustors, e.g. diesel engines and gas turbines, pressures much higher than atmospheric are present. LII measurements at elevated pressure have been performed in diesel engines [19–24] at peak pressures up to 70 bar. Engines are, however, systems with strongly varying conditions and are not suitable for fundamental LII investigations at elevated pressure. In order to apply LII quantitatively under these conditions, systematic studies in stable, laminar flames in high-pressure environments are necessary. So far, few experimental studies have been performed under stable high-pressure conditions: soot volume fractions were measured in premixed, ethylene/air flames up to 5 bar [25] as well as in a methane/air diffusion flame up to 25 bar [26]. Effective particle diameters were determined in a methane/air diffusion flame up to 40 bar [27], and a general study on LII at elevated pressure was performed in a premixed, ethylene/air flame up to 15 bar [28]. At atmospheric pressure the obtained particle sizes from LII data were compared to results from independent measurements, e.g. transmission electron microscopy (TEM) [29–31]. A similar comparison at elevated pressure to investigate the applicability of LII for quantitative soot particle sizing under these conditions has not been per-

✉ Fax: +49-203-379-3087, E-mail: thomas.dreier@uni-due.de

formed so far. In this context the question arises about which assumptions for modeling the LII signal variation are best suited for high-pressure conditions.

Therefore, the aim of this study is:

1. to set up a high-pressure burner that provides laminar, premixed sooting flames at elevated pressure.
2. to set up an LII model that combines commonly used submodels for different heat-conduction regimes.
3. to investigate particle sizing with LII at high-pressure conditions and
4. to compare particle sizes obtained with LII at elevated pressure with a second, independent method.

In the following sections, the theoretical and experimental approach to these aims will be described.

## 2 Experimental

### 2.1 *The high-pressure burner*

In order to experimentally investigate the LII technique at elevated pressure, a burner was constructed that was laid out to stabilize laminar, sooting premixed ethylene/air flames at pressures up to 10 bar. Compared to the burner used in previous studies [28], the optical access to the flame was improved and the use of a circular flame holder compared to a rectangular one will simplify future modelling of soot formation in premixed high pressure flames. The burner is installed inside a high-pressure chamber equipped with four fused silica windows arranged at 90° in a horizontal plane for optical access. The burner matrix consists of a disc of sintered metal foam of stainless steel (Siperm R10, 20 mm diameter). The central burner (premixed ethylene/air, sooting flame) is surrounded by a second burner (premixed methane/air, non-sooting flame) with a diameter of 56 mm that is made of a sintered bronze disc (Siperm® B40) in which a water-purged copper tube is embedded. The concept of a shielding flame has been successfully used before [32–37]. The surrounding, non-sooting flame prevents an oxidation of the central, sooting flame at the edges and avoids the steep temperature gradient between the hot sooting flame and the cold surrounding gas. Additionally, the surrounding flame stabilizes the central sooting flame, which is important as sooting flames are very sensitive and prone to flickering at elevated pressure. A funnel with several concentric rings is placed at 31 mm above the central burner to stabilize the flame and to ensure a laminar flow of the exhaust gases. The two burners are surrounded by a ring of sintered bronze (Siperm B40) through which a co-flow of air is led to further stabilize the flame and to keep the windows clean of soot and water deposition. All gas flows were controlled by mass-flow controllers (Bronkhorst). Ethylene and methane were taken from gas cylinders (Air Liquide), high-pressure air was provided by a compressor (Bauer Kompressoren). The exhaust gases of the burner were filtered in two stainless steel vessels to remove the soot. Finally, the exhaust gases pass a valve and the gases are expanded to atmospheric pressure. The entire burner is placed on a three-dimensional translation system. This provides the ability to probe the flame in all dimensions without the need of changing the alignment of the laser and the detection system. In this study experiments were conducted at 1, 2, 5 and 10 bar, and pressure fluctuation was less than ±2% for all investigated pressures. The conditions of the flames at the different pressures are listed in Table 1. Photographs of the flames at the given pressures are shown in Fig. 1. The flame has a diameter of ∼ 18 mm and a height of ∼ 30 mm. Although soot volume fractions were not measured in this study, it can be assumed that they are in the same range as the similar flame in [28], i.e. between 1 and 10 ppm.

| Pressure [bar] | Central burner $\Phi$ | Central burner $v_{fg}$ [cm/s] | Surrounding burner $\Phi$ | Surrounding burner $v_{fg}$ [cm/s] |
|---|---|---|---|---|
| 1 | 2.1 | 8 | 1.4 | 10 |
| 2 | 2.1 | 8 | 1.2 | 10 |
| 5 | 1.95 | 8 | 1.2 | 6 |
| 10 | 1.95 | 6 | 1.2 | 6 |

**TABLE 1** Equivalence ratio ($\Phi$) and fresh gas velocity ($v_{fg}$) for the central (ethylene/air) and the surrounding burner (methane/air) at 1, 2, 5, and 10 bar

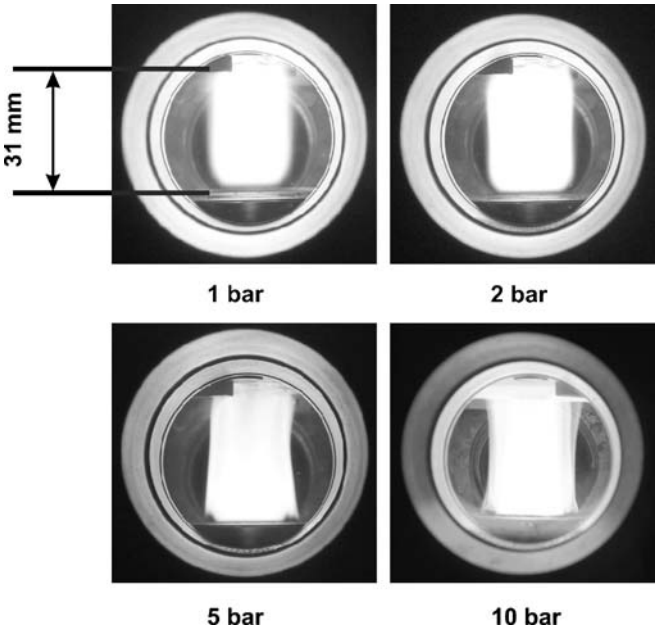


**FIGURE 1** Photographs of the flame at 1, 2, 5, and 10 bar

### 2.2 *LII detection*

For the LII experiment the beam of a pulsed Nd:YAG laser (Continuum PowerLite) at 1064 nm (Pulse duration: 7 ns FWHM) was horizontally aligned through the burner. An aperture with 2 mm diameter was used to select a homogeneous part of the laser beam which was then relay-imaged onto the center of the flame. In this way, a spatial near-top-hat beam profile was obtained. The spatial profile was measured using the knife-edge method and is shown in Fig. 2. In order to avoid evaporation of soot, low laser fluences (70–115 mJ/cm$^2$) were used to heat up the soot particles. The LII signal was detected both spectrally and temporally resolved. The spectrally-resolved detection at 400–650 nm was accomplished with an imaging spectrometer (Acton Research Corp., Model 150, grating with 100 grooves/mm, blazed for 450 nm) combined with an intensified CCD camera (ICCD) (FlameStar II, LaVision, 576 × 384 pixel, 12 bit). The inten-

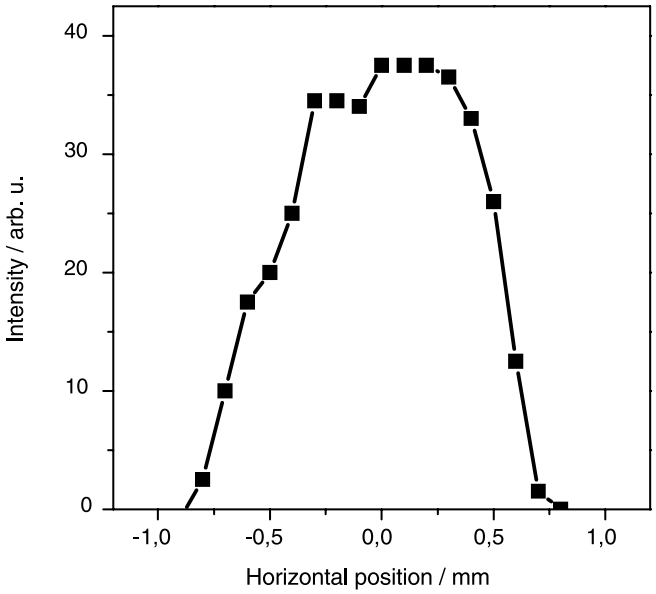


**FIGURE 2** Spatial laser-beam profile

sifier was gated for the first 40 ns of the LII signal. The combination of spectrometer and ICCD was calibrated for spectral sensitivity with a calibrated tungsten filament lamp (Spectra Physics Oriel, SN 7 ∼ 1545). The wavelength position was calibrated with a mercury lamp. The spectrometer with an ICCD camera was also used to measure the spectrally-resolved soot emission at flame temperature without laser heating. The time-resolved LII signal was detected at right angle to the laser beam at the burner's centerline with fast photomultipliers (Hamamatsu R7400U-04) at 550 and 694 nm, respectively. The spectral width of the interference filters was

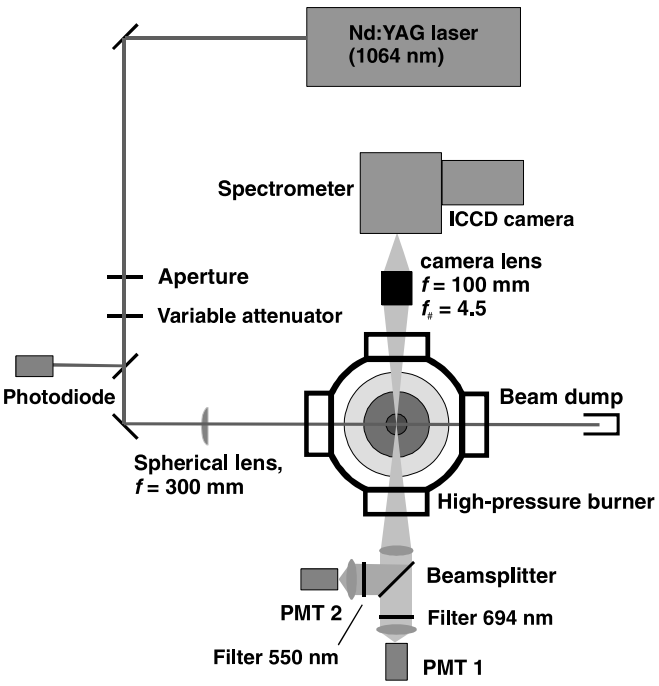


**FIGURE 3** Experimental setup. PMT: photomultiplier tube. ICCD: intensified charged coupled device

694 ± 12 and 550 ± 10 nm FWHM respectively. The combination of photomultipliers and filters was calibrated for spectral sensitivity with the same lamp as used for the spectrometer. The LII signals were recorded with a digital oscilloscope (LeCroy, 300 MHz, 2.5 GS, 170 pulses average) and transferred to a PC for further data evaluation. Data were taken at the burner's centerline from 4–20 mm height above the burner (HAB) in steps of 2 mm by vertically shifting the complete burner relative to the optical setup. The signal is averaged over a height of 2 mm due to the dimensions of the laser beam. The experimental setup is shown in Fig. 3.

### 2.3 *TEM probe sampling*

Samples from the flame soot were collected for TEM analysis. A device was constructed which enabled thermophoretic sampling at elevated pressure. One of the windows of the burner was replaced by the sampling device. No significant change to the flame was observed with this modification. A sluice was constructed that enabled multiple sampling while the burner was running at constant pressure. The vertical position could be varied in order to take samples at different heights above the burner surface. A rod was equipped with two thin metal sheets holding a TEM grid of carbon coated copper with a diameter of 3 mm each. The rod with the TEM grid was inserted manually into the flame which resulted in a sampling time of approximately half a second. O-rings around the rod ensured sealing against the pressure difference. The grid was inserted parallel to the flow of the flame to minimize disturbances. Soot was deposited thermophoretically on the grid. Soot samples were collected from the flame at 10 and 20 mm height above the burner surface, respectively. Care was taken to ensure that the samples were taken from the same measurement volume as the LII measurements. The grids were collected through the sluice while the flame was burning at constant, high pressure: the rod with the TEM grid was pulled out of the flame, a valve was closed between the flame and the grid, and in the last step, the rod was pulled through the sealing o-rings around the rod. A Philips transmission-electron microscope (Model CM 12) was used to analyze the samples. Images of the samples were recorded by a CCD camera (1024 × 1024 pixels, 8 bit) and stored for further data analysis.

## 3 Modeling LII

Numerous models for the prediction of the temporal behavior of the LII signal have been developed [12, 24, 38–43]. The basis for most models is an energy and mass balance that considers the absorption of laser energy as well as heat loss due to vaporization of material from the surface, heat conduction to the surrounding gas, and radiation. This energy balance can be written as

$$\dot{Q}_{\mathrm{abs}} = \dot{Q}_{\mathrm{int}} + \dot{Q}_{\mathrm{evap}} + \dot{Q}_{\mathrm{cond}} + \dot{Q}_{\mathrm{rad}}\,, \tag{1}$$

where $\dot{Q}_{\mathrm{abs}}$ is the energy flux of laser absorption, $\dot{Q}_{\mathrm{int}}$ is the change in internal energy, $\dot{Q}_{\mathrm{evap}}$ is the energy flux due to evaporation, $\dot{Q}_{\mathrm{cond}}$ the energy flux related to heat conduction and $\dot{Q}_{\mathrm{rad}}$ the heat loss due to radiation. A more detailed model for soot particles including thermal annealing and oxidation

has been developed by Michelsen [44]. If the laser energy is sufficient to heat the particle above the vaporization threshold, carbon fragments will evaporate from the particle surface which will result in a mass loss of the particle and an increase of mass in the gas phase. This mass balance is described as

$$\frac{\mathrm{d}m_\mathrm{p}}{\mathrm{d}t} = J_\mathrm{evap}\,, \tag{2}$$

with the particle mass $m_\mathrm{p}$, the time $t$ and the mass flux $J_\mathrm{evap}$. The resulting coupled differential equations (1) and (2) can be solved numerically and yield the particle temperature and particle diameter as a function of time. The particle temperature is then turned into LII signal intensities using Planck's law. In the present study, only particle cooling is modelled in order to obtain particle sizes from experimental LII decay curves. The absorption term is, therefore, set to zero.

### 3.1 *Change in internal energy*

The change in internal energy is given by

$$\dot{Q}_\mathrm{int} = m_\mathrm{p} c_\mathrm{p,s} \frac{\mathrm{d}T_\mathrm{p}}{\mathrm{d}t}\,, \tag{3}$$

where $T_\mathrm{p}$ is the particle temperature. The molar heat capacity of soot $c_\mathrm{p,s}$ is expressed empirically in dependence on the particle temperature:

$$c_\mathrm{p,s} = \frac{a_\mathrm{c,s} + b_\mathrm{c,s} T_\mathrm{p} + \frac{c_\mathrm{c,s}}{T_\mathrm{p}^2}}{M_\mathrm{s}}\,, \tag{4}$$

where $a_\mathrm{c,s}$, $b_\mathrm{c,s}$ and $c_\mathrm{c,s}$ are empirical constants and $M_\mathrm{s}$ is the molar mass of the particle [24].

### 3.2 *Heat conduction*

Heat conduction depends on the local gas-kinetic conditions that can be divided into three regimes: the free-molecular regime, the continuum regime and the transition regime. The discrimination between these regimes is important when discussing LII with respect to the pressure influence. At typical flame temperatures of $\sim 1700\,\mathrm{K}$ and atmospheric pressure, heat conduction from the soot particles to the surrounding gas takes place in the free-molecular regime. With increasing pressure, heat conduction gradually shifts towards the continuum regime, i.e. heat conduction takes place in the transition regime. An estimation from Liu et al. [45] shows that the conditions for continuum heat conduction are very unlikely in LII, as in that case particle sizes must be very large, gas temperatures very low, and pressures extremely high. Therefore, this study takes into account the free-molecular heat-conduction regime as well as two heat-conduction models for the transition regime.

### 3.3 *Free-molecular regime*

In the free-molecular regime, heat conduction is dominated by molecule–particle collisions. In the case of a particle in an infinite bath gas, heat conduction can be described by

$$\dot{Q}_\mathrm{cond,FM} = \alpha\pi d_\mathrm{p}^2 \frac{p}{8}\sqrt{\frac{8RT_\mathrm{g}}{\pi M_\mathrm{g}}}\frac{\gamma^*+1}{\gamma^*-1}\left(\frac{T_\mathrm{p}}{T_\mathrm{g}}-1\right), \tag{5}$$

where $d_\mathrm{p}$ is the primary particle diameter, $R$ is the universal gas constant, $p$ is the gas pressure, $\alpha$ is the thermal accommodation coefficient, $M_\mathrm{g}$ is the molar mass of the gas, and $T_\mathrm{g}$ is the gas temperature. FM indicates free-molecular conditions. The average heat capacity ratio $\gamma^*$ is defined by Filippov and Rosner [46] as

$$\frac{1}{\gamma^*-1} = \frac{1}{T_\mathrm{p}-T_\mathrm{g}}\int_{T_\mathrm{g}}^{T_\mathrm{p}} \frac{\mathrm{d}T}{\gamma-1}\,, \tag{6}$$

with the heat capacity ratio $\gamma = c_\mathrm{p}/c_\mathrm{v}$ of the surrounding gas. In order to calculate $\gamma$ of the gas, the temperature-dependent heat capacity of the gas $c_\mathrm{p,g}$ is required. It is given by

$$c_\mathrm{p,g} = a_\mathrm{c,g} + b_\mathrm{c,g} T_\mathrm{g} + \frac{c_\mathrm{c,g}}{T_\mathrm{g}^2}\,, \tag{7}$$

where $a_\mathrm{c,s}$, $b_\mathrm{c,s}$ and $c_\mathrm{c,s}$ are empirical constants [24].

### 3.4 *Transition regime*

*3.4.1 Transition regime: McCoy and Cha.* A commonly-used heat conduction model for LII in the transition regime was given by Melton [38]. It is based on the work of McCoy and Cha [47] who derived the following expression for two concentric spheres in the transition regime:

$$\dot{Q}_\mathrm{cond,Trans} = \frac{2k_\mathrm{g}(T_\mathrm{g})\pi d_\mathrm{p}^2 (T_\mathrm{p}-T_\mathrm{g})}{d_\mathrm{p} + G\lambda_\mathrm{MFP}}\,, \tag{8}$$

Here, the mean free path in the gas is

$$\lambda_\mathrm{MFP} = \frac{k_\mathrm{g}(T_\mathrm{g})}{f(T_\mathrm{g})p}\left(\gamma(T_\mathrm{g})-1\right)\sqrt{\frac{\pi M_\mathrm{g} T_\mathrm{g}}{2R}}\,. \tag{9}$$

In (8) the factor $G$ at gas temperature is

$$G = \frac{8f}{\alpha(\gamma+1)}\,, \tag{10}$$

in which the Eucken factor $f$ [48] is

$$f = (9\gamma-5)/4\,. \tag{11}$$

The thermal conductivity of the surrounding gas $k_\mathrm{g}$ is temperature dependent. In this work, the expression given by Michelsen [44] for air has been used:

$$k_\mathrm{g} = h_1 + h_2 T_\mathrm{g} \tag{12}$$

where $h_1$ and $h_2$ are empirical constants.

The model of McCoy and Cha can be used for all heat-conduction regimes as it provides a smooth transition between the free-molecular and the continuum regime.

*3.4.2 Transition regime: Fuchs' approach.* Fuchs' approach [49, 50] is based on the assumption that heat conduction from a particle to the surrounding gas in the transition regime can be divided into two zones. The inner zone is a sphere of thickness $\delta$ around the particle with $\delta$ in the order of the mean free path length of the gas molecules. Inside this zone heat conduction is assumed to follow the mechanisms of the free-molecular flow, whereas outside the limiting sphere heat conduction takes place according to the continuum regime. The particle has the temperature $T_\mathrm{p}$, the temperature inside the limiting sphere is $T_\delta$ and outside the sphere the gas has the temperature $T_\mathrm{g}$.

The key point in using the Fuchs model is to find the values for the thickness of the boundary layer and the temperature inside this limiting sphere. Filippov and Rosner [46] describe the required equations to calculate $\delta$ and $T_\delta$. The thickness of the limiting sphere can be calculated as

$$\delta = \frac{(d_\mathrm{p}/2)^3}{\lambda_{\mathrm{MFP},\delta}^2}\left(\frac{1}{5}\Lambda_1^5 - \frac{1}{3}\Lambda_2\Lambda_1^3 + \frac{2}{15}\Lambda_2^{\frac{5}{2}}\right) - \frac{d_\mathrm{p}}{2}\,, \tag{13}$$

with the mean free path inside the sphere $\lambda_{\mathrm{MFP},\delta}$ and the coefficients

$$\Lambda_1 = 1 + \frac{\lambda_{\mathrm{MFP},\delta}}{d_\mathrm{p}/2}\,; \quad \Lambda_2 = 1 + \left(\frac{\lambda_{\mathrm{MFP},\delta}}{d_\mathrm{p}/2}\right)^2\,. \tag{14}$$

The mean free path inside the sphere can be calculated with equation (9) with $T_\delta$ instead of $T_\mathrm{g}$. Hence, with known pressure and molecular mass of the gas, $\delta$ is a function of temperature in the boundary layer only. The heat conduction inside the boundary layer is expressed by (5) and (6) with $T_\delta$ instead of $T_\mathrm{g}$:

$$\dot{Q}_{\mathrm{cond,FM}} = \alpha\pi d_\mathrm{p}^2 \frac{p}{8}\sqrt{\frac{8RT_\delta}{\pi M_\mathrm{g}}}\frac{(\gamma^*+1)}{(\gamma^*-1)}\left(\frac{T_\mathrm{p}}{T_\delta} - 1\right)\,. \tag{15}$$

Heat conduction outside the limiting sphere follows the model for the continuum regime. The 'particle diameter' is the diameter of the boundary layer, i.e. the radius is $\delta + d_\mathrm{p}/2$. With the expression for continuum heat conduction [46] one obtains for the heat conduction outside the sphere

$$\dot{Q}_{\mathrm{cond,C}} = 4\pi\left(\delta + d_\mathrm{p}/2\right)\int_{T_\mathrm{g}}^{T_\delta} k_\mathrm{g}\,\mathrm{d}T\,. \tag{16}$$

The next step is to obtain $T_\delta$. As there are no sources or sinks for heat, (15) and (16) must be equal. With that relation $T_\delta$, and successively $\delta$, can be determined by numerically solving the combination of expressions. Then, the heat conduction in the transition regime can be calculated by using either (15) or (16).

### 3.5 *Vaporization*

The heat-loss term for vaporization is based on the model of Snelling et al. [51] and is described in [43]. In the present study, low laser fluences are applied and, thus, the influence of vaporizing soot is negligible. Nevertheless, the vaporization term is included in the model.

### 3.6 *Radiation*

The heat loss due to radiation follows the Stefan–Boltzmann law. The emitted power over all wavelengths is

$$\dot{Q}_\mathrm{rad} = \pi d_\mathrm{p}^2 \theta \sigma_\mathrm{B}\left(T_\mathrm{p}^4 - T_\mathrm{g}^4\right)\,. \tag{17}$$

Here, $\sigma_\mathrm{B}$ is the Stefan–Boltzmann constant and $\theta$ the total emission coefficient. Assuming black-body radiation, $\theta$ is set to 1. This is a simplified expression, as soot is not a perfect black body. The difference is, however, negligible at atmospheric pressure and above, as radiation contributes little to the total heat loss under these conditions.

### 3.7 *Polydisperse particle sizes*

In most cases, the primary particles detected within the probe volume are not monodisperse. This will have a significant impact on the LII signal as the cooling of the laser-heated particles strongly depends on their size. The temperature decay of an ensemble of polydisperse primary particles will be the integral of the individual cooling curves of the different particle sizes within the probe volume. It has been shown that for hydrocarbon flames at atmospheric and elevated pressure [32] the primary particle-size distribution follows a log-normal function given by

$$df = \frac{1}{\sqrt{2\pi}d_\mathrm{p}\ln\sigma_\mathrm{g}}\exp\left[-\frac{(\ln d_\mathrm{p} - \ln \mathrm{CMD})^2}{2\left(\ln\sigma_\mathrm{g}\right)^2}\right]\mathrm{d}d_\mathrm{p}\,. \tag{18}$$

The distribution is characterized by the count median diameter CMD and the geometric width $\sigma_\mathrm{g}$. $df$ is the probability to find a particle size between $d_\mathrm{p}$ and $d_\mathrm{p} + \mathrm{d}d_\mathrm{p}$. The distribution is not symmetric but has a long tail towards larger particles.

### 3.8 *Influence of aggregates*

In real systems, nano-sized particles tend to stick together and form aggregates. Taking into account the effect of aggregation in modeling LII is a fairly new topic. It was introduced for the first time by Filippov et al. [52]. They describe a "shielding"-effect: particles inside an aggregate are shielded against the gas molecules by surrounding particles. This results in a decreased heat transfer for aggregated primary particles compared to single, isolated particles and thus a slower LII signal decay.

The LII model modifications for aggregates were presented for the first time by Snelling et al. [29] and were improved by Liu and coworkers [53, 54]. In the present study, the aggregate model of Liu et al. was used. The primary particle size is allowed to be log-normal, whereas the aggregate size, for reasons of simplification, was assumed to be monodisperse, i.e. a constant number of primary particles per aggregate was assumed.

### 3.9 *Final LII signal*

With the above described sub-models, (1) and (2) are solved numerically with a fourth-order Runge–Kutta algorithm. This yields the temperature, the particle diameter, as well as the relative contributions of the different heat-loss

| Property | Value | Source |
|---|---|---|
| $\lambda_{ex}$ | 1064 nm | |
| $E(m)$ | 0.4 | [29] |
| FWHM (laser) | 7 ns | |
| $\varrho_p$ | 1860 kg m$^{-3}$ | [24] |
| $M_s$ | 0.012011 kg mol$^{-1}$ | Molecular mass of carbon |
| $a_{c,s}$ | 22.5566 J mol$^{-1}$ K$^{-1}$ | [24] |
| $b_{c,s}$ | 0.0013 J mol$^{-1}$ K$^{-2}$ | [24] |
| $c_{c,s}$ | − 1819.5 kJ K mol$^{-1}$ | [24] |
| $\alpha$ | 0.25 | This study |
| $M_g$ | 28 g mol$^{-1}$ | Molecular mass of nitrogen |
| $a_{c,g}$ | 28.58 J mol$^{-1}$ K$^{-1}$ | [24] |
| $b_{c,g}$ | 0.00377 J mol$^{-1}$ K$^{-2}$ | [24] |
| $c_{c,g}$ | −50 kJ K mol$^{-1}$ | [24] |
| $h_1$ | $1.08 \times 10^{-2}$ W m$^{-1}$ K$^{-1}$ | [44] |
| $h_2$ | $5.15 \times 10^{-5}$ W m$^{-1}$ K$^{-2}$ | [44] |

**TABLE 2** Physical properties used for the LII model

mechanisms as a function of time. Finally, the LII signal intensity is calculated from the particle temperature using Planck's law for near black-body particles. Hence, the contribution to the measured LII signal from each particle in the detection volume is given by

$$S_{\mathrm{LII}} = 2\pi^2 h c^2 d_p^2 \times \int_{\lambda_1}^{\lambda_2} \Omega(\lambda)\varepsilon(\lambda) \left[ \frac{1}{\lambda^5 \left[ \exp\left(\frac{hc}{\lambda k_B T_p}\right) - 1 \right]} - \frac{1}{\lambda^5 \left[ \exp\left(\frac{hc}{\lambda k_B T_g}\right) - 1 \right]} \right] \mathrm{d}\lambda \,, \quad (19)$$

with the Planck constant $h$, the speed of light $c$, the Boltzmann constant $k_B$, the spectral response function of the detection system $\Omega$, and the spectral emissivity of soot $\varepsilon$. The emissivity is related to the absorption cross-section $C_{abs}$ and is given by [44]

$$\varepsilon = \frac{4C_{abs}}{\pi d_p^2} = \frac{4\pi d_p E(m)}{\lambda_{det}} \,. \quad (20)$$

The signal is integrated over the detection bandpass from $\lambda_1$ to $\lambda_2$. The physical properties used in the LII model are listed in Table 2. This LII model is used for the evaluation of the experimental LII signals recorded at high-pressure conditions.

## 4 Results and discussion

### 4.1 *Flame temperature*

In order to evaluate the time-resolved LII signals with respect to the particle size, the flame temperature is required as an input value for the LII model. Therefore, two-color soot pyrometry was used to determine the flame temperature from the spectrally-resolved thermal emission without laser heating. The signal was extracted from the emission spectra at $530 \pm 5$ nm and $640 \pm 5$ nm. From the ratio of the signals at the two wavelengths $\lambda_1$ and $\lambda_2$ the particle temperature (assumed in thermal equilibrium with the gas temperature) can be calculated according to

$$T_g = \frac{hc}{k_B} \left( \frac{1}{\lambda_2} - \frac{1}{\lambda_1} \right) \left[ \ln \left[ \frac{S_{soot}(\lambda_1 T_g)}{S_{soot}(\lambda_2 T_g)} \frac{C_2 \lambda_2}{C_1 \lambda_1} \frac{\varepsilon \lambda_2 \lambda_1^5}{\varepsilon \lambda_1 \lambda_2^5} \right] \right]^{-1} , \quad (21)$$

where $k_B$ is the Boltzmann constant, $S_{soot}$ is the detected emission signal, and $C_1$ and $C_2$ are calibration constants that account for the spectral sensitivity of the spectrometer and the detector at the two wavelengths. Finally, $\varepsilon$ is the emissivity of the particles. The emissivity is a function of the refractive index of soot. The absolute value of $E(m)$, which is not known in detail [55], is not required; only the ratio of $E(m)$ at the two detection wavelengths is needed. The ratio $\varepsilon(\lambda_2)/\varepsilon(\lambda_1)$ can be approximated by $\lambda_1/\lambda_2$ assuming that $E(m)$ is constant between the two wavelengths. The flame temperatures are shown in Fig. 4. It should be noted that the flame temperature is an average value along the line of detection as the spectral soot emission is not spatially resolved like that from techniques relying on laser-induced signals. Temperatures are biased towards the highest temperature because the signal light is dominated by radiation from particles with the highest temperature and, hence, the strongest emission. The temperatures increase slightly from 1–5 bar. For these measurements, the fresh-gas velocity was fixed at 8 cm/s. The mass-flow rates thus increase linearly with pressure and more fuel is burned at higher pressure in the same volume – resulting in higher flame temperatures. For 10 bar, a slower fresh gas velocity of 6 cm/s was used and, hence, the temperatures are lower than those at 5 bar. With increasing height above the burner, the temperature decreases slowly. The main reaction zone is located within the first few millimeters above the burner surface and the reaction heat is released in that region. The reaction products are then carried to higher heights and cool down, resulting in the slow temperature decay. As will be described in the following section, in this series of experiments the relatively high temperature in the 5 bar flame will have an impact on the primary particle size.

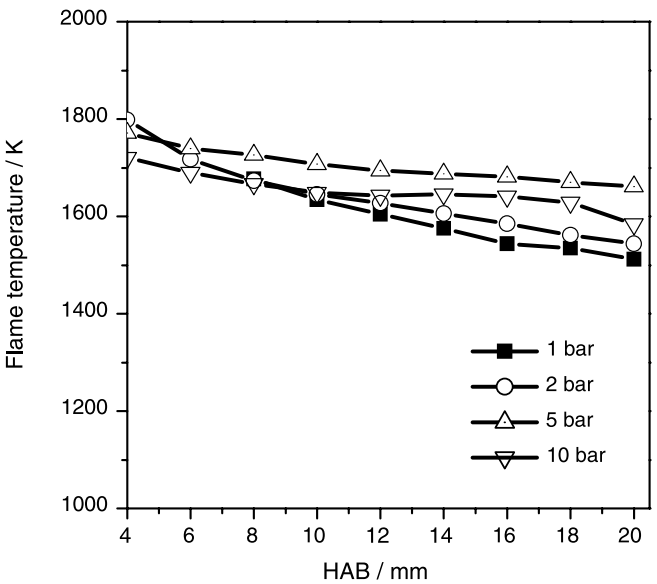


**FIGURE 4** Flame temperature obtained from pyrometry of soot emission as a function of height above the burner

### 4.2 *TEM analysis of soot samples*

Representative TEM images of the soot samples collected in the flame at 20 mm height above the burner surface are shown in Fig. 5. All images are shown for a magnification of 40 000, the scale is given in the figure. The primary particles are loosely connected and form aggregates at all pressures. The smallest particles can be observed at 5 bar. The particle size depends mainly on temperature; with increasing temperature, particles become smaller. The flame temperature at 5 bar was higher compared to the other pressures – resulting in smaller particles at this pressure. The primary soot particle size was measured in several TEM images. The obtained diameters were divided into classes of the same primary particle size. In such a way, a histogram was obtained which shows the number of particles (counts) per particle-size class. The histograms were then fitted by a log-normal particle-size distribution with the mean diameter, the geometric width and an intensity scaling parameter as free fit parameters. A log-normal distribution fits the particle sizes well for all investigated pressures. The histograms and best fits for soot samples collected at 20 mm HAB are shown in Fig. 6. The same evaluation with similar results was performed for the samples taken at 10 mm HAB.

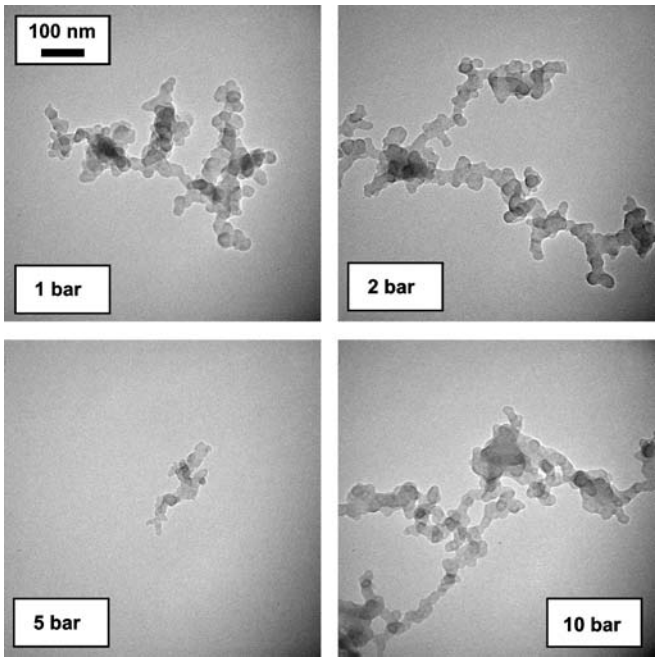


**FIGURE 5** TEM images from soot samples for 1–10 bar (typical examples) collected at 20 mm HAB

### 4.3 *LII particle sizing in the high-pressure burner*

*4.3.1 Spectrally-resolved detection of LII.* Emission from the $C_2 d^3\Pi_g \rightarrow a^3\Pi_u$ Swan bands has been reported to interfere with the LII signal at high laser power densities, and even emission from OH and O atoms have been observed with 532-nm excitation [56]. $C_2$ Swan-band emission appears at 473 nm ($\Delta v = +1$), 516 nm ($\Delta v = 0$), 563 nm ($\Delta v = -1$), and 618 nm ($\Delta v = -2$). Hence, potential interferences in the 550 nm detection channel used in this study can be expected. To investigate any narrow-band emissions resulting from fluorescing species, the LII signal was detected and spectrally resolved at all pressures. LII emission spectra detected at

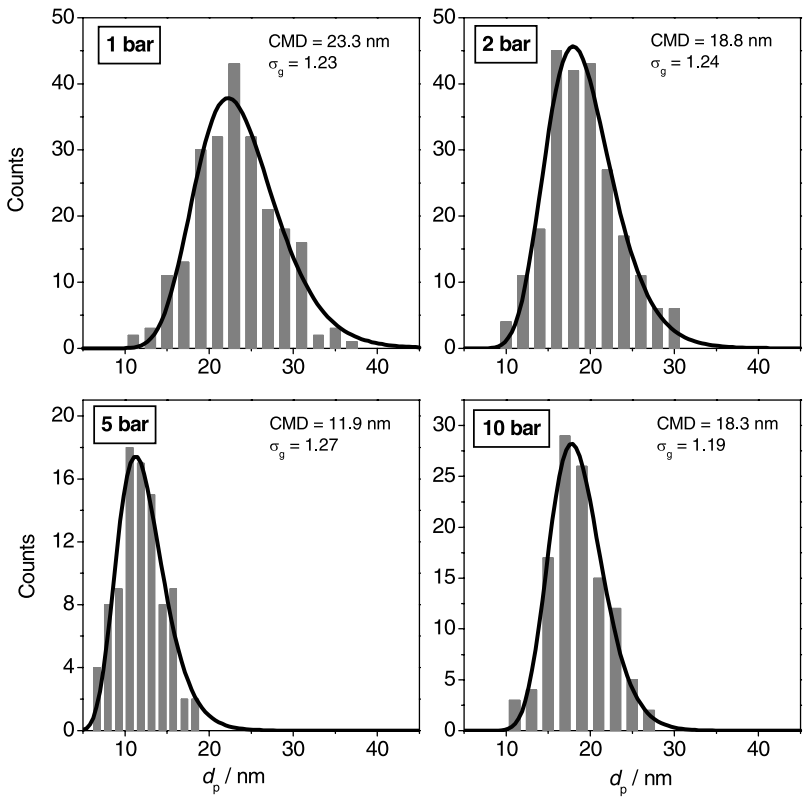


**FIGURE 6** Primary particle sizes counted in TEM-images (*gray bars*) with best log-normal fit (*black line*) obtained from TEM-images of soot at 20 mm HAB

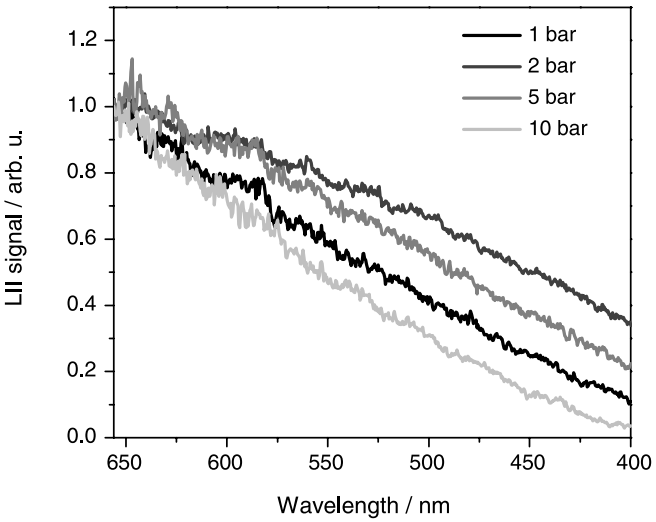


**FIGURE 7** Spectrally-resolved LII signal for 1–10 bar at 20 mm HAB. The signals are normalized at 656 nm

20 mm HAB are shown in Fig. 7. The spectra have been normalized at 656 nm. No interference of narrow-band emissions can be seen in the region between 656 and 400 nm for all investigated pressures. Small ripples result from not entirely suppressed streaks in the background of the CCD image. The reason for the absence of interferences is the low laser fluence of $< 115\,\mathrm{mJ/cm^2}$ used in this study. Interferences were reported for much higher fluences at 1064 nm excitation ($153\,\mathrm{MW/cm^2}$) [56]. Second, the spatial distribution of the laser fluence is near top hat avoiding locally high peak fluences. Gaussian fluence distributions result in high peak values in the center, even if the average laser fluence as measured by a power meter is relatively low. Therefore, in the case of higher fluences and inhomogeneous laser beam profiles one should avoid LII detection wavelengths that are nearby a Swan band emission.

*4.3.2 Time-resolved LII detection and particle sizing.* Typical time-resolved LII signals for 1 bar and 10 bar are shown in Fig. 8. The LII signal at 10 bar decreases much faster than the signal at 1 bar due to the increased heat conduction with elevated pressure. The intensity of the LII signal at 550 nm is higher than the signal at 694 nm due to the higher sensitivity of the detection system at shorter wavelengths. For the data evaluation of the LII signals with respect to the particle-size distribution, the peak particle temperature after laser heat-up was calculated from the ratio of the two LII signals detected at $\lambda_1$ and $\lambda_2$. The LII signal decay, which contains the particle-size information, is simulated and fitted to experimental decay curves. The LII model requires the peak particle temperature as start value for the particle cooling. This simplifies the simulation as the absorption term can be set to zero. Using (21), the peak particle temperature $T_\mathrm{p}^0$ can be calculated from the peak signals $S_\mathrm{p}(\lambda_1, T_\mathrm{p}^0)$ and $S_\mathrm{p}(\lambda_2, T_\mathrm{p}^0)$ at the two wavelengths. As in the case of the measurement of the flame temperature, the absolute value of $E(m)$ is not required, but only the ratio of $E(m)$ at the two detection wavelengths. Care was taken to use low laser fluences and to avoid evaporation of soot since the

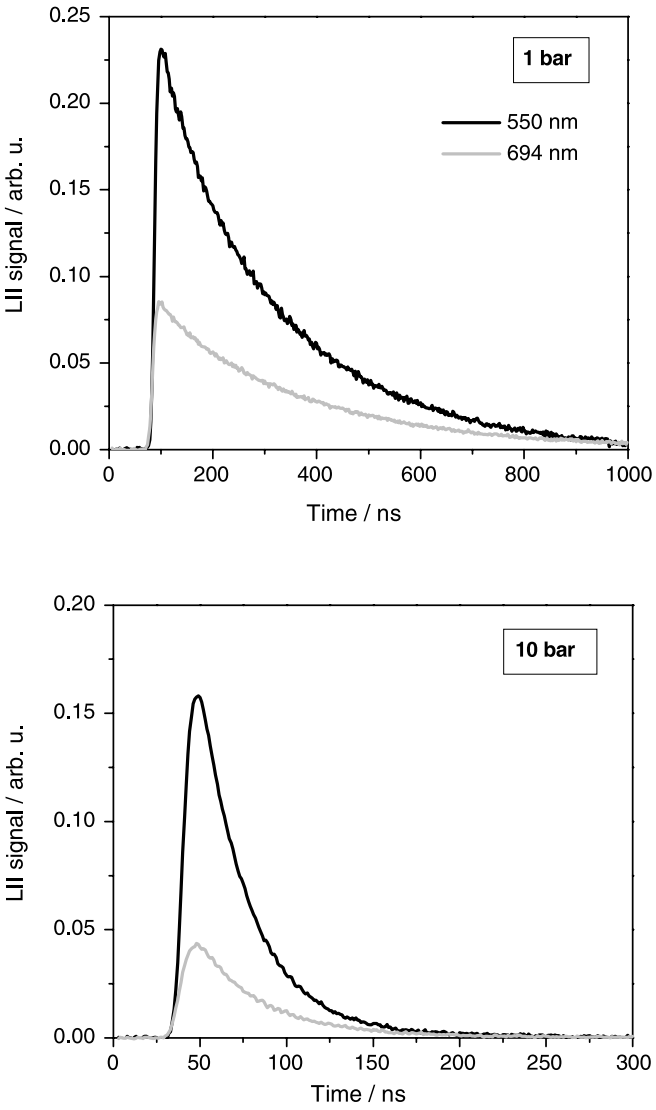


**FIGURE 8** Time-resolved LII signals (170 pulse averages) at 1 bar (**a**) and 10 bar (**b**) detected at 550 nm and 694 nm at 20 mm HAB. Note the different time scales of the horizontal axis

vaporization term in the LII model introduces additional uncertainty. The obtained peak particle temperatures are below 3500 K for all pressures which is well below the vaporization temperature of 3915 K at atmospheric pressure. If for simplification thermal equilibrium is assumed during particle heating, the vaporization temperature should even increase with increasing pressure due to the Clausius–Clapeyron relation. Therefore, also for the high-pressure case, soot vaporization should be negligible for peak particle temperatures below 3500 K.

The LII signal at 550 nm was taken for evaluating the particle-size distribution as it is the stronger signal with the better signal-to-noise ratio. The section of the signal trace before the peak, i.e. the particle heating period, was disregarded assuming no overlap between the particle heat-up and the cooling process. This assumption is acceptable for short laser pulses (7 ns), even for the 10 bar case where the LII signal decay is still long ($\sim 200$ ns) compared to the laser pulse. To guarantee no overlap between heating and cooling, the LII

signal was fitted starting 26 ns after the signal peak at 1 bar and 13 ns after the peak for 2–10 bar. The peak particle temperature calculated with (21) is the particle temperature at this position. The simulated LII signals were fitted to the experimental LII decay curves with the count median diameter CMD and the width $\sigma_g$ of the log-normal particle-size distribution as free fit parameters. The gas-phase temperatures obtained from soot pyrometry of non-laser heated soot were used as input for the gas temperature required by the LII model. Four different models for conduction were compared: the free-molecular model, the two-layer model of Fuchs, the model of McCoy and Cha, and the Fuchs model combined with the reduced heat conduction due to aggregated particles. A certain aggregate size, i.e. a number of primary particles per aggregate, had to be assumed. From the TEM images shown in Fig. 5 it can be seen that the aggregates contain in general at least 50 primary particles. However, it is difficult to asses the exact number of primary particles from the TEM images. Additionally, the aggregate size varies, like the primary particle size, and is probably log-normally distributed as well. Assuming an aggregate-size distribution would, however, introduce two new, unknown parameters. Hence, for simplification a constant, monodisperse aggregate size of 100 primary particles per aggregate was assumed for all cases. It is evident from the study of Snelling et al. [29] that the largest reduction in heat conduction for aggregates is given for the transition from a single particle towards 20–50 primary particles per aggregate. The reduction in heat conduction, levels off for aggregates larger than 50-100 primary particles per aggregate. Even if aggregates with more than 100 primary particles per aggregate were present in the measurement volume, this would have a minor effect only.

Examples for best fits to experimental LII decay curves recorded at 20 mm HAB are shown in Fig. 9 for the four investigated gas pressures. With increasing pressure the signals decay faster due to increased heat conduction. Calculations were performed using the Fuchs model combined with the aggregation model. The experimental LII signal decays are normalized to 1 at the start of particle cooling. The other models result in excellent fits as well. The mean diameters that are obtained from the fits, however, are significantly different. For clarity, the 5 bar trace is plotted for an expanded time scale shown on the upper horizontal axis in Fig. 9. Otherwise, the 5 and 10 bar traces would virtually fall on top of each other. Since the LII signal decay time is influenced by both pressure and particle size this means that for the 5 bar flame the particles are smaller than for the 10 bar flame. The evaluated particle diameters, taken from the compilations presented in Fig. 10 below, are listed in the insert of the figure.

The count median particle diameters that are obtained with the different heat conduction sub-models are shown as function of height above the burner surface in Fig. 10 including the results of the TEM analysis. In all cases, the particle sizes increase gradually with height above the burner until they reach a constant size. This is typical for sooting, premixed flames as the fuel is decomposed shortly after the burner exit and soot particles are built up with increasing height above the burner until the flame chemistry is finished. With increasing pressure, the particles reach their final size earlier, i.e. at lower heights above the burner, as the density increases with pressure.

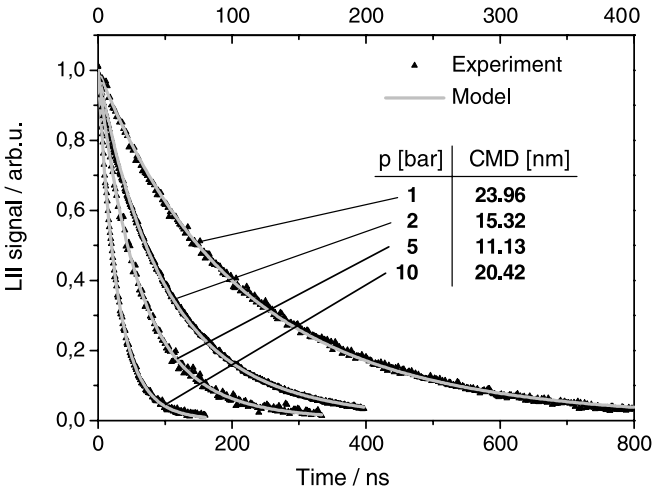


**FIGURE 9** Numerical fits (*grey solid lines*) to experimental LII decay curves (*symbols*) detected at 550 nm at 20 mm HAB. The results for the 5 bar case are plotted with respect to the upper time axis (see text). The calculated profiles are shown for the Fuchs model taking into account the effect of aggregation. The evaluated count mean diameters are indicated in the legend

From Fig. 10 it is obvious that the development of the mean particle size with pressure in the different flames investigated does not follow a general trend with increasing pressure, especially when comparing the 1 and 2 bar flames with the 5 and 10 bar flames. We believe that this behavior was the result of the two higher pressure flames being operated with different equivalence ratios (cf., Table 1) and/or gas flow velocities than the two lower pressure flames, also leading to somewhat higher flame temperatures than the two lower pressure flames (cf., Fig. 4). These non-uniform experimental conditions within the set of flames investigated here can cause different soot formation histories and thus particle size developments with pressure and height above the burner as revealed here by TR-LII.

Comparing different LII sub-models the results of the free-molecular model and the Fuchs model are almost identical up to 5 bar. Only slight differences can be seen at 10 bar. Heat conduction, therefore, seems to take place in the free-molecular regime up to 10 bar. Of course, the free-molecular heat-conduction model accounts for increased heat conduction with increasing pressure (5). Particle sizes are slightly smaller if the McCoy and Cha model for heat conduction is applied. The smallest particle sizes are obtained with the Fuchs model combined with the aggregation model. Simulated LII signals for aggregates decrease slower due to decreased heat conduction (shielding effect). Hence, in the inverse case of fitting an experimental LII decay curve including the aggregation model, the evaluation leads to smaller primary particle sizes. The comparison of the LII data evaluation with different heat-conduction sub-models with the TEM-image analysis shows a good agreement for all pressures when using the Fuchs model combined with the aggregation model. This is the first time, that the LII aggregation sub-model is tested in a practical situation, where particle sizes are deduced using this sub-model.

To investigate the sensitivity of the evaluation on experimental parameters, i.e. the peak particle temperature obtained from two-color LII and the gas-phase temperature obtained

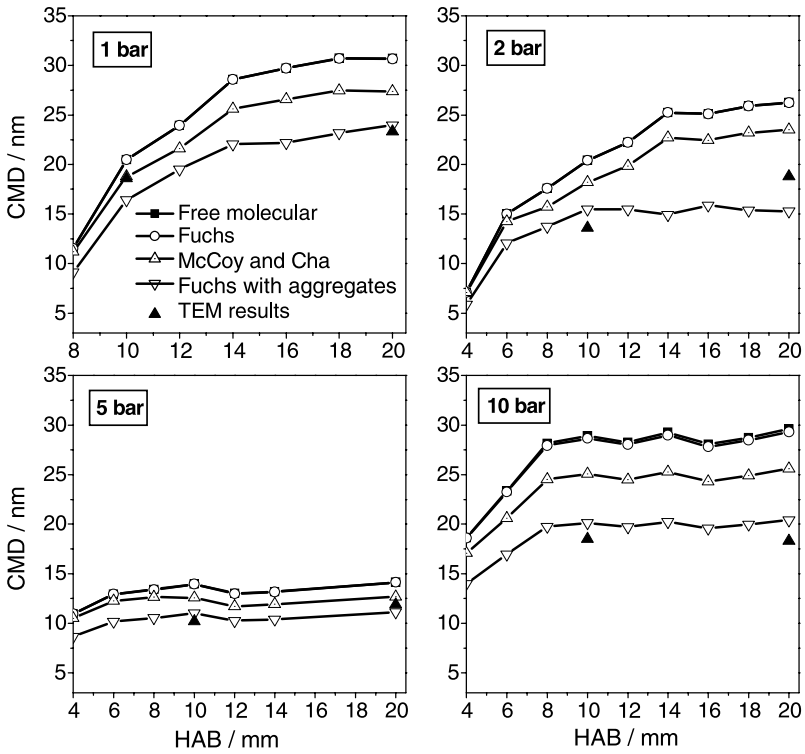


**FIGURE 10** Evaluated count median diameter (CMD) of the log-normal primary particle-size distribution as a function of height above the burner (HAB) for 1–10 bar. The results are shown for the free-molecular heat conduction model (*solid squares*), Fuchs' model (*open circles*), the McCoy and Cha model (*open triangles tip up*), and Fuchs' model combined with the aggregate model with the assumption of 100 primary particles per aggregate (*open triangles tip down*). The *solid triangles* show the results of the TEM analysis

from pyrometry, a ±10% change for these values was assumed and the evaluation was repeated for these conditions for the case of the Fuchs model with aggregation. The result is shown in Fig. 11 for the 10 bar case. The influence on the obtained median particle diameter is less than 10% for a variation in $T_p^0$ and $T_g$. This indicates that even with the assumption of 10% errors in the experimental input the Fuchs model with the aggregation sub-model is in best agreement with the TEM results for all pressures. This best agreement was obtained for a value of 0.25 for the thermal accommodation coefficient. If higher values were used, like 0.3 used in [43, 44] or 0.37 in [29], neither model yielded good agreement with the TEM results as all particle sizes obtained from LII were too large. Therefore, all evaluations were done for a thermal accommodation coefficient of 0.25. A typical value of 0.3 resulted in slightly to high particle diameters, even for the Fuchs model with aggregation.

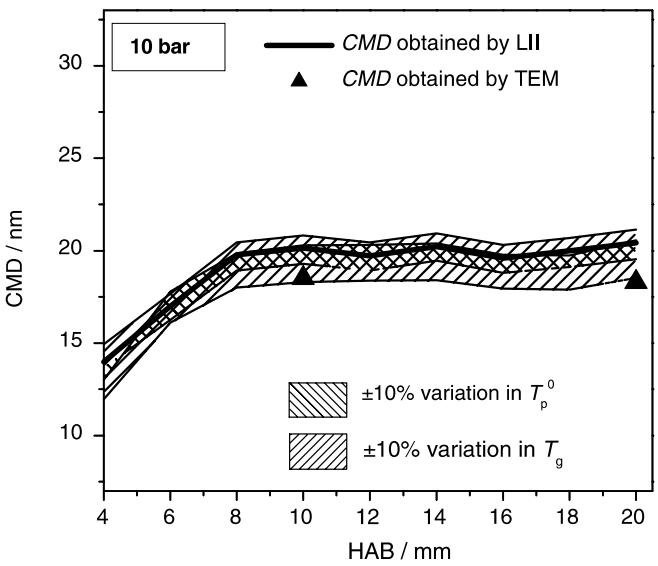


**FIGURE 11** Sensitivity of the experimentally obtained count median diameter at 10 bar to a ±10% variation in assumed peak particle temperature $T_p^0$, and to a ±10% variation in assumed gas-phase temperature $T_g$. The analysis is based on the Fuchs' model with 100 primary particles per aggregate (*thick solid line*). The TEM results are shown as *solid triangles*

The results for the width $\sigma_g$ of the particle-size distribution are more sensitive to a change in $T_p^0$ and $T_g$. For $\sigma_g$, no model can be determined that matches the TEM results best. Assuming a ±10% change in $T_p^0$ and $T_g$ causes a variation of $\sigma_g$ determined by LII (Fuchs model with aggregation) of $\sim \pm 13\%$.

Our results identify the Fuchs model combined with the aggregation sub-model as the best LII model to determine the mean particle size of a log-normal particle-size distribution in the range of 1–10 bar. It should be noted, however, that other models can obtain similar results for the CMD by adjusting the physical parameters, e.g. the soot density, the thermal accommodation coefficient, the heat-capacity ratio $\gamma$, or the heat capacity. In this work, however, we used the physical assumptions that are based on recent theoretical investigations [45, 54]. Further research, both in modeling LII (like a more detailed influence of aggregation on the LII signal) and experiments at pressures larger than 10 bar are required to clarify the correct experimental approach and data reduction and to determine the applicability of LII for the measurement of particle-size distributions for a broad pressure range.

## 5 Conclusions

The log-normal size distribution of soot particles was measured in a newly developed sooting high-pressure

burner at pressures of 1–10 bar using time-resolved laser-induced incandescence (LII). The high-pressure burner stabilizes premixed, laminar sooting ethylene/air flames up to 10 bar.

Spectrally-resolved LII signals showed no interferences of $C_2$ Swan band emissions up to 10 bar with low laser fluences ($< 115\,\mathrm{mJ/cm^2}$) at 1064 nm excitation. The mean primary particle size of a log-normal particle-size distribution was determined from time-resolved LII using different models for heat conduction. At all pressures studied a thermal accommodation coefficient of 0.25 in the heat conduction model was shown to best describe the size distributions evaluated from fits to experimental LII decay profiles compared with those determined by TEM-analysis. The use of different models results in different particle sizes. In order to resolve which model assumptions are best suited for our conditions, soot samples were collected at two different positions in the flame at all investigated pressures. The samples were analyzed by transmission electron microscopy (TEM). For the first time, soot primary particle-size distributions obtained from LII were compared with a second, independent method at elevated pressures. The results show good agreement of the mean diameter of the particle-size distribution obtained by TEM analysis and LII for all pressures if the LII data are evaluated with the Fuchs model, taking into account the reduced heat conduction of aggregated particles.

**ACKNOWLEDGEMENTS** The authors gratefully acknowledge the Deutsche Forschungsgemeinschaft (DFG) for the financial support within SCHU1369/3, W. Weis, K. Schmitt (Heidelberg), and K. Pape (Göttingen) for technical support and Profs. H.G. Wagner (Göttingen) and J. Wolfrum (Heidelberg) for their continuous interest and support.

## REFERENCES

1 T. Ni, J.A. Pinson, S. Gupta, R.J. Santoro, Appl. Opt. **34**, 7083 (1995)
2 D.J. Bryce, N. Ladommatos, H. Zhao, Appl. Opt. **39**, 5012 (2000)
3 B. Quay, T.-W. Lee, T. Ni, R.J. Santoro, Combust. Flame **97**, 384 (1994)
4 R.L. Vander Wal, Appl. Phys. B **59**, 445 (1994)
5 J. Appel, B. Jungfleisch, M. Marquardt, R. Suntz, H. Bockhorn, Proc. Combust. Inst. **26**, 2387 (1996)
6 B. Axelsson, R. Collin, P.-E. Bengtsson, Appl. Opt. **39**, 3683 (2000)
7 B. Axelsson, R. Collin, P.-E. Bengtsson, Appl. Phys. B **72**, 367 (2001)
8 H. Geitlinger, T. Streibel, R. Suntz, H. Bockhorn, Proc. Combust. Inst. **27**, 1613 (1998)
9 T.R. Meyer, S. Roy, V.M. Belovich, E. Corporan, J.R. Gord, Appl. Opt. **44**, 445 (2005)
10 H. Bockhorn, H. Geitlinger, B. Jungfleisch, T. Lehre, A. Schön, T. Streibel, R. Suntz, Phys. Chem. Chem. Phys. **4**, 3780 (2002)
11 S. Will, S. Schraml, A. Leipertz, Proc. Combust. Inst. **26**, 2277 (1996)
12 S. Will, S. Schraml, K. Bader, A. Leipertz, Appl. Opt. **37**, 5647 (1998)
13 T. Lehre, B. Jungfleisch, R. Suntz, H. Bockhorn, Appl. Opt. **42**, 2021 (2003)
14 D. Woiki, A. Giesen, P. Roth, Proc. Combust. Inst. **28**, 2531 (2000)
15 R.L. Vander Wal, T.M. Ticich, A.B. Stephens, Combust. Flame **116**, 291 (1999)
16 B.F. Kock, T. Eckhardt, P. Roth, Proc. Combust. Inst. **29**, 2775 (2002)
17 C. Schulz (Ed.), Laser-induced incandescence: Quantitative Interpretation, Modeling, Application, Intl. Bunsen Discussion Meeting and Workshop, Vol. 195, CEUR Workshop Procs. http://CEUR-ws.org/Vol-195/, Duisburg, Germany (2005)
18 C. Schulz, B.F. Kock, M. Hofmann, H. Michelsen, S. Will, B. Bougie, R. Suntz, G. Smallwood, Appl. Phys. B **83**, 333 (2006)
19 J.E. Dec, C. Espey, SAE Technical Paper Ser. No. 950456 (1995)
20 G. Bruneaux, D. Verhoeven, T. Baritaud, SAE Technical Paper Ser. No. 1999-01-3648 (1999)
21 D. Choi, M. Iwamuro, Y. Shima, J. Senda, H. Fujimoto, SAE Technical Paper Ser. No. 2001-01-1255 (2001)
22 K. Inagaki, S. Takasu, K. Nakakita, SAE Technical Paper Ser. No. 1999-01-0508 (1999)
23 J.A. Pinson, D.L. Mitchell, R.J. Santoro, T.A. Litzinger, SAE Technical Paper Ser. No. 932650 (1993)
24 B.F. Kock, B. Tribalet, C. Schulz, P. Roth, Combust. Flame **147**, 79 (2006)
25 K.P. Geigle, Y. Schneider-Kühnle, M.S. Tsurikov, R. Hadef, R. Lückerath, V. Krüger, W. Stricker, M. Aigner, Proc. Combust. Inst. **30**, 1645 (2005)
26 L.L. McCrain, W.L. Roberts, Combust. Flame **140**, 60 (2005)
27 K.A. Thomson, D.R. Snelling, G.J. Smallwood, F. Liu, Appl. Phys. B **83**, 469 (2006)
28 M. Hofmann, W.G. Bessler, C. Schulz, H. Jander, Appl. Opt. **42**, 2052 (2003)
29 D.R. Snelling, F. Liu, G.J. Smallwood, Ö.L. Gülder, Combust. Flame **136**, 180 (2004)
30 A. Boiarciuc, F. Foucher, C. Mounaïm-Rousselle, Appl. Phys. B **83**, 413 (2006)
31 M. Charwath, R. Suntz, H. Bockhorn, Appl. Phys. B **83**, 435 (2006)
32 T. Heidermann, H.H. Jander, H.G. Wagner, Phys. Chem. Chem. Phys. **1**, 3497 (1999)
33 H. Böhm, C. Feldermann, T. Heidermann, H. Jander, B. Lüers, H.G. Wagner, Proc. Combust. Inst. **24**, 991 (1992)
34 S. Hanisch, H. Jander, T. Pape, H.G. Wagner, Proc. Combust. Inst. **25**, 577 (1994)
35 H. Böhm, D. Hesse, H. Jander, B. Lüers, J. Pietscher, H.G. Wagner, M. Weiss, Proc. Combust. Inst. **22**, 403 (1988)
36 M. Bönig, C. Feldermann, H. Jander, B. Lüers, G. Rudolph, H.G. Wagner, Proc. Combust. Inst. **23**, 1581 (1990)
37 H. Mätzing, H.G. Wagner, Proc. Combust. Inst. **21**, 1047 (1986)
38 L.A. Melton, Appl. Opt. **23**, 2201 (1984)
39 D.R. Snelling, F. Liu, G.J. Smallwood, Ö.L. Gülder, Evaluation of the nanoscale heat and mass transfer model of LII: Prediction of the excitation intensity, 34th Nat. Heat Transfer Conf., Pittsburgh (2000)
40 D.L. Hofeldt, SAE Technical Paper Ser. No. 930079 (1993)
41 H. Bladh, P.-E. Bengtsson, Appl. Phys. B **78**, 241 (2004)
42 B. Mewes, J.M. Seitzman, Appl. Opt. **36**, 709 (1997)
43 H.A. Michelsen, F. Liu, B.F. Kock, H. Bladh, A. Boiarciuc, M. Charwath, T. Dreier, R. Hadef, M. Hofmann, J. Reimann, S. Will, P.-E. Bengtsson, H. Bockhorn, F. Foucher, K.-P. Geigle, C. Mounaïm-Rousselle, C. Schulz, R. Stirn, B. Tribalet, R. Suntz, Appl. Phys. B **87**, 503 (2007)
44 H.A. Michelsen, J. Chem. Phys. **118**, 7012 (2003)
45 F. Liu, K.J. Daun, D.R. Snelling, G.J. Smallwood, Appl. Phys. B **83**, 355 (2006)
46 A.V. Filippov, D.E. Rosner, Int. J. Heat Mass Transf. **43**, 127 (2000)
47 B.J. McCoy, C.Y. Cha, Chem. Eng. Sci. **29**, 381 (1974)
48 S. Chapman, T.G. Cowlings, *Mathematical Theory of Non-Uniform Gases* (Cambridge Univ. Press, London, 1970)
49 N.A. Fuchs, Geophys. Pura Appl. **56**, 185 (1963)
50 N.A. Fuchs, *The Mechanics of Aerosols* (Pergamon, Oxford, 1964) (Dover, New York, 1989)
51 D.R. Snelling, F. Liu, G.J. Smallwood, Ö.L. Gülder, Proceedings of NHTC, 34th Nat. Heat Transfer Conf., Pittsburgh, Pennsylvania, paper no. NHTC2000-12132 (2000)
52 A.V. Filippov, M. Zurita, D.E. Rosner, J. Colloid Interf. Sci. **229**, 261 (2000)
53 F. Liu, G.J. Smallwood, D.R. Snelling, J. Quant. Spectrosc. Radiat. Transf. **93**, 301 (2005)
54 F. Liu, M. Yang, F.A. Hill, D.R. Snelling, G.J. Smallwood, Appl. Phys. B **83**, 383 (2006)
55 K.C. Smyth, C.R. Shaddix, Combust. Flame **107**, 314 (1996)
56 R.L. Vander Wal, K.J. Weiland, Appl. Phys. B **59**, 445 (1994)